IEEE Access
Multidisciplinary ⋮ Rapid Review ⋮ Open Access Journal

Received 10 January 2024, accepted 25 January 2024, date of publication 30 January 2024, date of current version 7 February 2024.

Digital Object Identifier 10.1109/ACCESS.2024.3360139

RESEARCH ARTICLE

HQMC-CPC: A Hybrid Quantum Multiclass Cardiac Pathologies Classification Integrating a Modified Hardware Efficient Ansatz

DOAA A. SHOIEB[1], AHMED YOUNES[2,3], SHERIN M. YOUSSEF[1], AND KARMA M. FATHALLA[1], (Member, IEEE)

[1]Computer Engineering Department, Arab Academy for Science, Technology and Maritime Transport (AASTMT), Alexandria 1029, Egypt
[2]Department of Mathematics and Computer Science, Faculty of Science, Alexandria University, Alexandria 21511, Egypt
[3]Alexandria Quantum Computing Group, Faculty of Science, Alexandria University, Alexandria 21511, Egypt

Corresponding author: Doaa A. Shoieb (doaa.shoieb@aast.edu)

ABSTRACT Cardiac pathology classification (CPC) based on the volumetric features of three key heart structures can be extracted from segmented cardiac cine magnetic resonance imaging (CMRI) sequences. Machine learning models have recently become very effective tools for handling these problems. Hybrid quantum methods can be employed to enhance the capacities of classical machine learning models. Here, we propose a hybrid quantum multiclass cardiac pathologies classification (HQMC-CPC) model. In the proposed model, discriminative features are extracted to characterize the shape and function of the heart, combining the clinical features, patient features, and radiomics features. In the proposed quantum circuits, all variational parameters are trainable, and the enhanced variational quantum circuit is employed for efficient neural network learning. Using only thirty feature values as input, we propose a hybrid quantum multiclass cardiac pathologies classification (HQMC-CPC) model based on the proposed modified hardware efficient ansatz (MHEA). The proposed model achieves promising results in training and testing with the Automatic Cardiac Diagnosis Challenge (ACDC 2017) dataset. Experimental results showed that the proposed HQMC-CPC model is able to classify different cardiac pathologies with an average minimum performance gap of 3.19%. The average maximum improvement in terms of accuracy in cardiac pathology classification is 7.77%. Moreover, the proposed HQMC-CPC speeds up the testing process by around 60% and 40% compared to the classical classifiers and well-established HEA respectively.

INDEX TERMS Ansatz, cardiac pathologies, classification, clinical features, quantum circuit, radiomic features.

I. INTRODUCTION

Cardiovascular diseases (CVDs) have become a major public health concern, and according to regular reports from the World Health Organization (WHO), they have been identified as the primary cause of death globally [1]. Characterization of CVDs is difficult because of the numerous compensatory mechanisms that may obstruct the effect directly associated with the disease [2]. The analysis of heart function is critical for the diagnosis of CVDs. CMRI of the heart is widely recognized as a critical modality for such analysis. Through non-invasive cardiac ventricle imaging, it facilitates the timely and accurate diagnosis of CVDs and helps in the early detection of cardiac dysfunction [3], [4]. CMRI is obtained during a cardiac cycle that alternates between a relaxing (diastole) and a contracting (systole) phase. Evaluations of the ventricles' masses, ejection fractions (EF), and volumes, known as clinical parameters, are frequently carried out at two intervals that mark the end of the diastole (ED) and systole phases (ES) [5].

The associate editor coordinating the review of this manuscript and approving it for publication was Sangsoon Lim.

Heart and blood vessel disorders are classified as cardiovascular diseases (CVD). It includes myocardial infarction (MINF), abnormal right ventricle (RV), and cardiomyopathies (CMPs) which are myocardial disease that causes heart failure (HF) and/or sudden cardiac death (SCD) worldwide. The initial morphological classification of CMPs included hypertrophic cardiomyopathy (HCM) and dilated cardiomyopathy (DCM). Heart muscle disease known as dilated cardiomyopathy usually starts in the left ventricle. In dilated cardiomyopathy, the ventricle lengthens and thins (dilates), resulting in a less efficient heart pump [6]. In hypertrophic cardiomyopathy, the ventricular septum develops. The term ''heart attack'' or ''myocardial infarction'' refers to the death of the heart muscle. Usually, it occurs when a blood clot partially or totally blocks a damaged blood vessel, reducing or stopping blood flow to a section of the heart and ultimately causing damage to the heart muscle [6]. Right ventricle hypertrophy (RVH) is the most common abnormality in the ventricle. It is a heart condition characterized by the thickening of the walls of the RV [7], [8] This scenario of little or no alterations challenges treatment personalization especially when considering how the heart structure evolves to maintain hemodynamic physiology [2]. Discriminative features are required to properly understand, analyze, and differentiate CVD. Moreover, early diagnosis of CVDs lowers the risk of sudden cardiac mortality in approximately 25% of CVDs patients and improves prognosis in other complex and asymptomatic CVDs [2].

Medical image classification has experienced massive advances in the era of deep learning using Convolutional Neural Networks (CNN) [9], [10] and vision transforms [11]. Recently, deep learning (DL) algorithms effectively classified CVDs in CMRI [2], [12], [13], [14], [15], [16], [17]. However, those algorithms are typically very complex and require a lot of time. Furthermore, CNN techniques still have limitations in medical applications, despite advancements in (DL), as datasets usually contain images with poor contrast or a limited number of samples. The advantages of quantum machine learning (QML) include speed and reduced parameter requirements. Furthermore, QML has emerged for quick information processing and enhances the approximation and generalization capabilities of classical neural networks [18], [19]. Additionally, quantum computing provides a new perspective on how machines identify patterns in data, whether they can learn from fewer training data, and their ability to generate new machine learning techniques. Moreover, quantum computers generate nontypical model patterns, which conventional computers are inefficient in their construction [19]. As a result, it is expected that quantum computers will outperform traditional computers in machine learning.

The majority of current cardiac pathology classification models use deep learning techniques that use redundant learning parameters, which results in poor classification performance. Moreover, some of the models stated [12], [13], [14], [16] don't consider various forms of cardiac discriminative features. Additionally, some of these models used 2D slices of the heart to obtain various features as needed [12], [13], [15], [20]. However, key geometric information characterizing adjacency in the 3D neighborhood was mostly lost, putting the heart's overall anatomical consistency at risk. To address these shortcomings, the proposed model in this paper is inspired by QML and different 3D cardiac discriminative features. First, a set of discriminative features consisting of clinical, patient data, and radiomics features are extracted from 3D cardiac MRI images. Then the extracted features pass through recursive feature elimination (RFE) to select the most effective features. Finally, an enhanced hardware-efficient ansatz (HEA) is implemented as a parametrized model for a variational quantum circuit (VQC) to improve the classification accuracy and speed up the classification process. As a result, the proposed model can achieve effective classification results, in terms of accuracy The proposed hybrid quantum classification model is motivated by the illustrated challenges, which impose limitations on the performance of the existing cardiac classification models. The contributions can be summarized as follows:

1. An enhanced lightweight version of hardware-efficient ansatz (HEA) with varying entanglement types and reduced rotation gates to lower computational complexity, improve efficiency and enable greater configuration flexibility.
2. Hybrid quantum multi-class cardiac pathology classification using a variational quantum circuit that classifies five classes using the hybrid classical-quantum approach.
3. A set of discriminative feature extraction includes radiomics and clinical features to describe the heart chamber volumes and myocardium motion patterns of the biventricular. Also helps in understanding the shape and tissue characteristics that help in the diagnosis of the patient's cardiac pathology.
4. A comparative analysis of the performances of established models in cardiovascular disease (CVDs) classification with the proposed model.

This paper is structured as follows: concepts and characteristics of qubits along with the most popular quantum gates and their usage in quantum machine learning are discussed. Then, similar studies that performed multiclass cardiac pathology classification are discussed, with a briefing of their shortcomings motivating further research. In addition, the state-of-the-art (SOTA) application of quantum classification in medical image analysis is briefly presented. In the methodology section, the benchmark datasets used to test the performance of the proposed model, along with proposed methodology are outlined. Also, the highlights of the proposed method and its components are depicted. The obtained results and the performance of HQMC-CPC are compared to existing approaches on the ACDC dataset in the Results section. Finally, the conclusion is drawn, and future work is presented.

II. QUANTUM BACKGROUND

Quantum computing implements quantum computer methods by employing the basic properties of quantum mechanics including superposition, coherence, decoherence, and entanglement [21], [22]. In classical computing, physical hardware uses binary logic, however, quantum computing has multiple levels. Multilevel systems can encode and process more information in a single quantum unit by having more states available. This has the potential to enable more complex computations and algorithms to be performed, resulting in increased computational power. Hence, a different state representation is needed and referred to as qubits.

A. CONCEPT OF QUBIT AND QUANTUM CHARACTERISTICS

The fundamental building block of quantum computing is referred to as a qubit and is denoted by Dirac notations |0> and |1> [21]. Another representation of the qubit is Bloch sphere representation where a geometrical representation for visualizing the state of a single qubit. Fig 1 shows that the z and -z axes represent the two qubit states |0> and |1> respectively. |0> state denotes an electron's upward spin, while |1> spin denotes an electron's downward spin. Any point $|\psi>$ on this sphere is represented by the equation $|\psi> = \alpha|0> + \beta|1>$, where α and β are complex number and $|\alpha|^2 + |\beta|^2 = 1$. Furthermore, the qubit state function on the Bloch sphere appears as a probability for the two qubit states |0> and |1>. The probability of $|0>$ *and* $|1>$ (α *and* β) is transformed into a form in Bloch sphere as shown in (1). Additionally, the probability of |1> can be expressed in complex numbers. The phenomenon of qubit can be in one state, zero state, or both states at the same time, known as linear superposition [23]. Qubit superposition provides a huge computational space that can be used to address a variety of challenging high-complexity problems [24]. Another important property of QC is entanglement. When qubits are entangled, their characteristics are linked. despite their physical separation. As a result, measuring one qubit changes the properties of the other qubits that are entangled with it. Entanglement is a valuable resource that can be used for dense coding and quantum modeling of coupled systems. Also, it is as though they speak a hidden language that transcends all boundaries [21], [24].

$$|\psi> = \cos(\frac{\theta}{2})|0> + e^{i\theta}\sin(\frac{\theta}{2})|1> \quad (1)$$

B. CONCEPT QUANTUM GATES

Quantum gates are the fundamental building blocks of large-scale quantum computers. The function of quantum gates is to conduct unitary operations that are reversible [24]. Table 1 illustrates some examples of quantum gates as well as their properties such as how they are represented, the number of qubits they operate on, their unitary matrix, and their description.

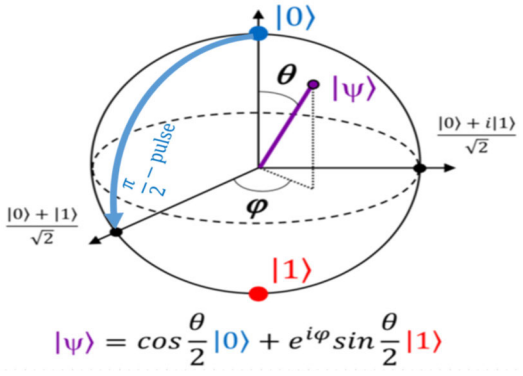

FIGURE 1. Block sphere representation of single qubit as it provides a convenient way to visualize the state of a single qubit and its operations. Any point on this sphere represents a complex linear combination of the 0 and 1 states [23].

C. QUANTUM MACHINE LEARNING

Quantum machine learning (QML) is a wide research field comprised of two main components: the data and the learning process. The various ways can be classified according to how the data is created and processed. There are four techniques for combining machine learning and quantum computing as depicted in Fig. 2: The data might be created by a quantum (Q) or classical (C) system. The processing device might be either quantum (Q) or classical (C).

The first type of QML is the use of quantum computers to speed up classical machine learning algorithms and known as classical/quantum hybrids, or CQ. The second type involves applying algorithms inspired by quantum mechanics to classical computers (QC). Finally, implementing quantum algorithms on quantum computers (QQ) is the third type [25]. Since the first category of QML techniques is more open and existing, it will be the focus of this paper.

QML is a training method that is expected to solve some of the limitations of classical ML by replacing neural network calculations with quantum computing [25]. QML applies quantum computing to ML by employing a Parametrized Variational Quantum Circuit (VQC), which mimics classical neural networks with fewer parameters [26]. Also, VQCs are the standard method for creating QNNs on the Noisy Intermediate-Scale Quantum (NISQ) devices that are currently available because they are susceptible to a lot of noise [25], [27]. VQC is the equivalent to classical NN made

Type of data \ Type of algorithm	Classical	Quantum
Classical	CC Classical ML	QC Quantum ML
Quantum	CQ Classical ML on quantum experiments	QQ Quantum-Quantum ML

FIGURE 2. Types of techniques for combining machine learning and quantum computing.

TABLE 1. Example of quantum gates.

Gate Name	No. of Qubits	Circuit Symbol	Unitary Matrix	Description
Pauli-X (NOT)	1	X	$\begin{pmatrix}0 & 1\\1 & 0\end{pmatrix}$	Analogous to classical NOT gate: Switches |0> to |1> and vice versa
Pauli-Y	1	Y	$\begin{pmatrix}0 & -i\\i & 0\end{pmatrix}$	Rotation through π radians around Bloch sphere y-axes.
Pauli-Z (phase flip)	1	Z	$\begin{pmatrix}1 & 0\\0 & -1\end{pmatrix}$	Rotation through π radians around Bloch sphere z-axes.
X-Rotation	1	$R_X(\theta)$	$\begin{pmatrix}\cos(\frac{\theta}{2}) & -isin(\frac{\theta}{2})\\-isin(\frac{\theta}{2}) & \cos(\frac{\theta}{2})\end{pmatrix}$	Rotates state vector about the Bloch sphere x-axes by θ
Y-Rotation	1	$R_Y(\theta)$	$\begin{pmatrix}\cos(\frac{\theta}{2}) & -sin(\frac{\theta}{2})\\-sin(\frac{\theta}{2}) & \cos(\frac{\theta}{2})\end{pmatrix}$	Rotates state vector about the Bloch sphere y-axes by θ
Z-Rotation	1	$R_Z(\theta)$	$\begin{pmatrix}e^{-i\frac{\theta}{2}} & 0\\0 & e^{\frac{\theta}{2}}\end{pmatrix}$	Rotates state vector about Bloch sphere z-axes by θ
Hadamard	1	H	$\frac{1}{\sqrt{2}}\begin{pmatrix}1 & 1\\1 & -1\end{pmatrix}$	Transform a basis state into an even superposition of the two basis states
CNOT: Controlled-not	2		$\begin{pmatrix}1 & 0 & 0 & 0\\0 & 1 & 0 & 0\\0 & 0 & 0 & 1\\0 & 0 & 1 & 0\end{pmatrix}$	The first qubit is known as the control qubit, and the second is the target qubit. When the control qubit is in state |1⟩|1>, the CNOT gate keeps the control qubit unmodified and executes a Pauli-X gate on the target qubit; when the control qubit is in state |0⟩|0⟩, the CNOT gate keeps the target qubit unmodified.

up of neurons and is composed of a set of quantum gates with trainable parameters. The hybrid QC approach used by the QML algorithm when it is implemented with VQC, as shown in Fig. 2, combines the use of quantum and classical devices. This technique prepares qubits and adjusts their quantum states using quantum gates by running the QNN model's quantum circuit on a quantum device. Fig. 3 illustrates that the quantum states are expressed by qubits once the datasets are encoded. These quantum states are fed into VQCs then the output quantum states are measured to reduce the probability distribution to a specific quantum state. Based on the qubit measurement results, changes to VQC's parameters are computed on a classical device using a classical optimizer. Finally, the output quantum states are converted into data that we can read and process. Fig.3 also elucidates the correspondence between the quantum circuit and the classical NN.

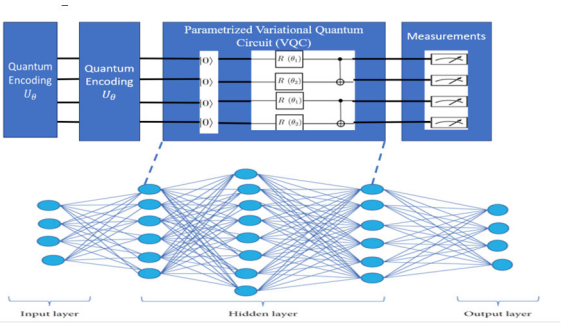

FIGURE 3. The structure correspondence of Parameterized Variational Quantum Circuit (VQC) and classical NN. The parameters and connections composing classical NN are mapped to the "Rotation gates and CNOT gates.

1) ENCODING TECHNIQUES

In a quantum system, data is represented using encoding. Processing on quantum devices requires encoding classical data into quantum states in Hilbert space [28]. Different types of encoding, such as basis, amplitude, and angle encoding, can be implemented and will be discussed in this section [28].

a: BASIS ENCODING

The basis encoding method is the simplest quantum encoding approach for arithmetic operations. Basis encoding encodes classical data in binary form before directly mapping it onto quantum computational bases. To do this, Pauli-X gates are used [28]. In general, the basis encoding approach loads the binary representation of a classical data point x = (x_1, x_2,……, x_n) into n qubits and encodes it as

$$|\Psi_x\rangle = \otimes_i^n |x_i\rangle \tag{2}$$

where ⊗ is tensor product operator. The limitation of this encoding approach is associated with the number of qubits, which is limited in NISQ computers.

b: AMPLITUDE ENCODING

The amplitude encoding approach encodes classical data into quantum state amplitudes. The amplitudes of log n-qubit quantum states are encoded to an n-dimensional normalized

classical vector $x = (x_1; x_2; \_\_\_ ; x_n)$ as

$$|\Psi_x \gg = \sum x_i |i> \quad (3)$$

where $|i>$ is the i-th computational basis state and $\sum |x_i|^2 = 1$

c: ANGLE ENCODING

The process of embedding data with rotational gates is known as angle encoding. The rotational gate that is used determines the final state, while the encoded value, or feature, is provided as an angle parameter. To encode the classical data in size n, n qubits, and n quantum rotation gates $R \in \{R_x, R_y, R_z\}$ are required. The angle encoding method produces a classical data instance $x = (x_1, x_2, \ldots, x_n)$ as

$$|\Psi_x \gg = \otimes_i^n R(x_i)|0> \quad (4)$$

To sum up, basis encoding and angle encoding requires are inefficient in terms of qubits required. In addition, basis encoding may not be able to capture complex non-linear relationships because it relies on explicit representation. Moreover, amplitude encoding may simply be preferred in the NISQ because it is very efficient in terms of the number of qubits, but it involves more complex operations and transformations, making it more difficult to implement and understand compared to angle encoding. Angle encoding captures non-linear relationships because angles in a high-dimensional space can have complex geometric relationships. Finally, for the proposed HQMC-CPC, angle encoding is selected as the required number of qubits can be implemented using NISQ and to take advantage of its non-linear relationships.

2) VARIATIONAL CIRCUIT (ANSATZ)

The ansatz, a parametrized variational quantum circuit, is used to generate a trial quantum state for a certain quantum algorithm or application. It determines the parameters and, thus, how they can be trained to reduce the cost, which is a crucial component of a VQC. In order to produce the desired quantum state, the ansatz consists of a number of quantum gates placed in a certain configuration. As illustrated in Fig. 4, $U(\theta)$ can be defined simply as the product of L sequentially applied unitaries. Moreover, some ansatz architectures can be used even in the absence of readily available pertinent information because they are generic and ''problem-agnostic''. Below, we list some of the ansatzes that are most frequently used in the literature.

a: HARDWARE EFFICIENT ANSATZ (HEA)

It is designed to be compatible with near-term quantum hardware, translating an arbitrary unitary into a sequence of gates, which is easily implementable in a device. It consists of alternating layers of single-qubit rotations and CNOT gates. The rotations are chosen to be simple and easy to implement, while the entangling gates are used to introduce quantum correlations into the circuit. Also, it aimed at reducing the

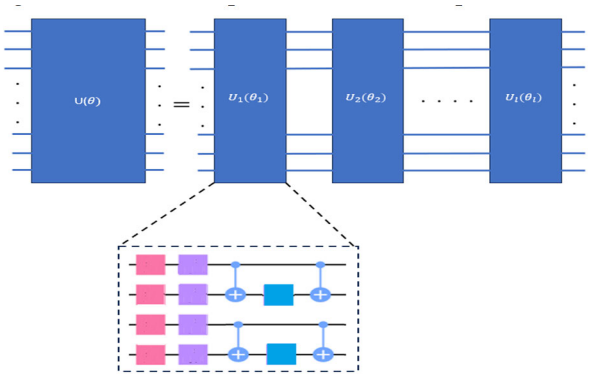

FIGURE 4. Schematic of the ansatz. It is possible to define the unitary $U(\theta)$ with θ as a product of L unitaries $U_l(\theta_l)$) working successively on an input state.

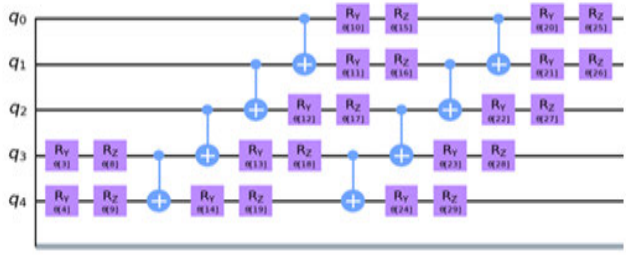

FIGURE 5. Hardware efficient ansatz for 5 qubits.

circuit depth needed to implement $U(\theta)$ when using a given quantum hardware. Fig 5 depicts the design of HEA in detail.

b: QUANTUM ALTERNATING OPERATOR ANSATZ (QAOA)

This ansatz is commonly used in optimization problems and consists of a series of single-qubit rotations and two-qubit interactions as depicted in Fig 6. The rotations are parameterized by angles that are optimized during the algorithm to find the optimal solution to the problem.

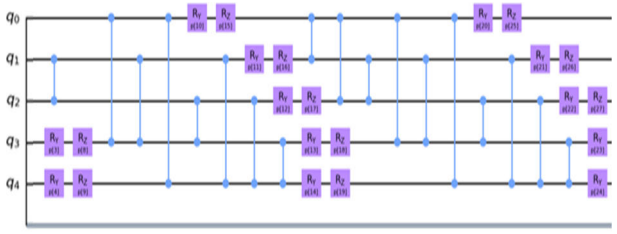

FIGURE 6. Quantum alternating operator ansatz for 5 qubits.

c: QUANTUM APPROXIMATE OPTIMIZATION ALGORITHM ANSATZ (QAOAA)

This ansatz is similar to QAOA but consists of a different set of single-qubit rotations and two-qubit interactions. The rotations and interactions are chosen to be compatible with the problem being solved. Fig 7 depicts the design of QAOAA in detail.

FIGURE 7. Quantum approximate optimization algorithm for 5 qubits.

d: VARIATIONAL QUANTUM EIGENSOLVER ANSATZ (VQE)

This ansatz is commonly used in finding the ground state energy of a Hamiltonian and consists of a circuit with a fixed number of layers of single-qubit rotations and entangling gates. The rotations are parameterized by angles that are optimized during the algorithm to find the optimal state. Fig 8 depicts the design of VQE in detail.

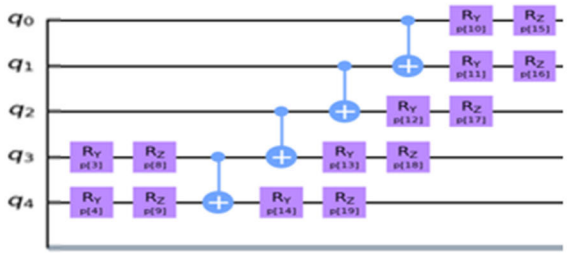

FIGURE 8. Variational quantum eigensolver ansatz for 5 qubits.

3) MEASUREMENTS

Measurements is the process of turning quantum information into classical bits. One important principle of quantum physics is that measurement results are probabilistic.

III. LITERATURE REVIEW

In this section, a twofold review of previous work is provided. First, related studies of cardiac pathology classification based on MRI images are discussed. In addition, the SOTA in medical image classification using Quantum Neural Network is presented. For analysis and classification of different cardiac pathologies, a web-based application model is presented by Huellebrand et al. [13] for semi-automated segmentation of the three cardiac structures using TL. Additionally, a set of 112 radiomics features have been extracted. Then, a Random Forest classifier was applied for cardiac pathology classification and achieved a maximum classification accuracy of 90%.

Also, Zheng et al. [14] contributed to cardiac pathology classification from cine cardiac MRI by a semi-supervised segmentation of the biventricular and extracting a set of motion features. Also, they applied binary classification by using four binary classifiers where each classifier works independently. They achieved 95% and 94% on the ACDC training set and testing set respectively as classification accuracy. Moreover, Ammar et al. [12] proposed a full pipeline for cardiac disease classification by employing UNet for segmentation and ensemble classifiers for classification. The disease prediction's accuracy reached 98% on the validation set and 92% on the test set. Additionally, Chang and Jung [16] applied two-step segmentation consisting of ROI localization by YOLO detector and FCN for segmentation. Moreover, a set of latent shape-related features has been extracted by point clouds and the classification accuracy was 92%.

Throughout the last few decades, quantum technology has been applied in a number of studies to improve classical machine learning performance. Various QML algorithms have emerged in recent years, with applications in classification, segmentation, regression, and reconstruction in medical image analysis (MIA). This section discusses recent techniques to introduce QML classification and their applications in MIA. As indicated in Table 2, various QML algorithms for classification problems have been developed in recent years. These algorithms are suitable for the prediction stage of medical image classification because they are more accurate and take less time to process than classical machine learning techniques.

The majority of previous work in this domain classified cardiac diseases using a simple TL or a single deep convolution neural network. The use of feature fusion and selection to combine different radiomics and clinical features is rarely described. The primary goal of this work was to develop an effective high-performing classification system using an enhanced VQC; at which complex feature analysis is investigated.

IV. MATERIAL AND METHODS

In this section, the data used for cardiac pathologies classification is described. Then, the proposed model architecture (HQMC-CPC) used for pathology classification is detailed. HQMC-CPC includes of three main phases to classify the four different cardiac pathologies and the normal one. The proposed architecture aims to provide a high-performance classification model with a minimum number of informative features, which aid the effective diagnosis of various pathologies. The first phase focuses on extracting different sets of discriminative features including clinical and radiomics features to accurately classify the different cardiac pathologies. Then, reducing the feature set by selecting the most effective features to feed into the quantum neural network to classify the pathology based on the input features. Finally, the selected features are encoded to be represented as quantum states and then passes through the proposed ansatz to classify the different cardiac pathologies as shown in Fig 9.

A. DATASET DESCRIPTION

The Automated Cardiac Diagnostic Challenge Dataset (ACDC 2017) [32] from the 2017 MICCAI challenge has been used in the experiments. The dataset contains clinical information from CMRI scans for 150 patients, comprising

TABLE 2. State-of-the-art application of quantum machine learning in medical image analysis.

Author	Paperwork	Scope	Dataset & Performance
Moradi et al. [29]	Quantum distance classifier (qDS) and a simplified quantum-kernel support vector machine (sqKSVM).	Binary classification	1. Pediatric Bone Marrow Transplant 2-year survival: accuracy: (sqKSVM :0.66, qDS: 0.64) 2. Wisconsin Breast Cancer Malign-vs-benign,: accuracy: (sqKSVM :0.88, qDS :0.91) 3. Heart Failure Mortality (sqKSVM: 0.50 , qDS :0.60)
Houssein et al [30]	Hybrid quantum-classical convolutional neural network (HQ-CNN)	Binary classification	Two private dataset: accuracy:0.98, recall:0.99, F1-measure:0.98, precision:0.99;
Amin et al [31]	VQC with ansatz consists of rotation gate, preceded by a succession of CNOT gates.	Multiclass classification	Kaggle: Accuracy: 98.03% BraTS0220: Accuracy :90.91% Local collected dataset: Accuracy :93.33%
Azevedo et al [32]	Hybrid classical quantum ResNet models using transfer learning	Binary classification	BCDR dataset: Precision:0.83; Recall:0.80; F1-score:0.81; Accuracy:0.81: Specificity:0.84
Amin et al [33]	VQC by inputting the divided images into the quantum circuit.	Binary classification	POF Hospital dataset : precision 0.94, accuracy: 0.94, recall 0.94, and F1-score 0.94. UCSD-AI4H/ COVID-CT precision: 0.96, accuracy :0.96, recall: 0.95, and F1-score : 0.96
Ovalle-Magallanes et al [34]	Stenosis detection using hybrid transfer-learning	Binary classification	Dataset: consisting of 250 X-ray coronary angiography accuracy: 0.91, precision: 0.88, recall 0.94, F1-score 0.91, specificity: 0.88

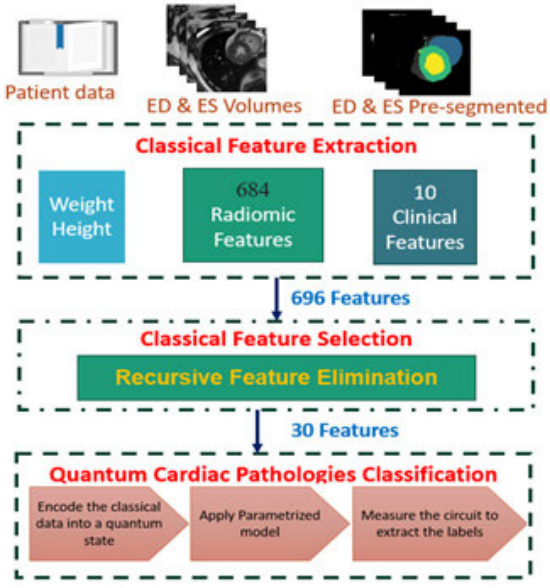

FIGURE 9. The proposed hybrid quantum multiclass cardiac pathologies classification (HQMC-CPC).

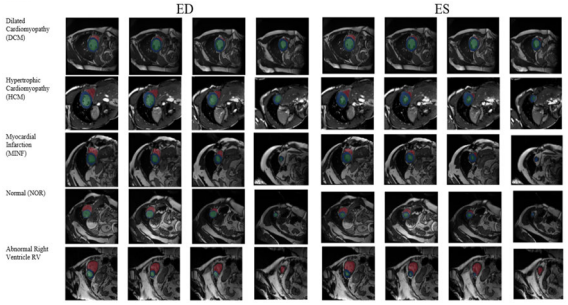

FIGURE 10. End-diastolic and end-systolic samples from the ACDC Dataset for the four distinct diseases and the normal heart (LV: green, RV: red, and Myo: blue) [37].

12-35 short-axis CMRI frames from both the ES and ED cardiac phases. One hundred and fifty patients had a clinical diagnosis; thirty patients from each of the five categories—normal (NOR), dilated cardiomyopathy (DCM), hypertrophic cardiomyopathy (HCM), myocardial infarction (MINF), and abnormal right ventricle (RV)—made up the 150 patients with a clinical diagnosis. Two MRI scanners with varying magnetic strengths—1.5 T (Siemens Area, Siemens Medical Solutions, Germany) and 3.0 T (Siemens Trio Tim, Siemens Medical Solutions, Germany)—were used to gather the data at the University Hospital of Dijon over six years. The spatial resolution of the biventricular short-axis slices is 1.37 1.68 mm2/pixel, with thicknesses ranging from 5 to 8 mm. The dataset additionally contains additional test subject data, such as diastolic-systolic phase instants, weights, and heights. In Fig. 10, samples from the dataset are shown.

B. CLASSICAL FEATURE EXTRACTION

A compromise between the best evaluation of the complex image data and a classification that is comprehensible for clinical experts may be possible when working with well-defined features [10], [33], [34]. So, the fusion between Clinical and Radiomics features assesses the anatomical and functional characteristics of the complex structure of the heart. Examples of clinical features are stroke volume, myocardium mass, LV and RV volume in both cardiac phases (ES and ED), and ejection fraction. Radiomics features describe the heart chamber volumes and myocardium motion patterns of the left and right ventricles. Moreover, they describe shape and texture based on the cardiac slice. Understanding the shape and tissue characteristics that assign a patient to a specific cardiac pathology is very helpful for generating hypotheses [35], [36].

1) CLINICAL FEATURES

Clinical features such as the volume and ejection fraction (EF) can provide valuable diagnostic, prognostic, and

treatment monitoring information in various cardiovascular diseases. They are useful tools for guiding treatment decisions, assessing disease progression, and monitoring therapeutic efficacy. Changes in LV and RV volumes and ejection fraction can occur in a variety of CVDs, such as heart failure, myocardial infarction, valvular heart disease, and pulmonary hypertension. The volumes of blood in the left ventricle in the cardiac cycle are dynamic and change with each heartbeat, depending on a variety of factors such as heart rate, contractility, preload, and afterload. Measurement of ED and ES LV volumes is an important diagnostic tool in the assessment of the function of LV. By comparing the volumes at these two points in the cardiac cycle, clinicians can calculate the ejection fraction, which is a measure of the percentage of blood that is ejected from the left ventricle during each heartbeat. While RV volume is an anatomical feature, it is also closely related to RV function. Changes in RV volume can be indicative of changes in RV function, as a healthy RV should be able to accommodate and eject blood efficiently. For example, an increase in RV volume can be a sign of RV dilation or dysfunction, while a decrease in RV volume can indicate RV atrophy or reduced cardiac output. Thus, while RV volume is primarily an anatomical feature, it is also a functional feature in the sense that it can provide important information about RV function and can be used to detect and monitor different CVDs affecting the RV, such as pulmonary hypertension, RV infarction, and arrhythmogenic right ventricular cardiomyopathy. The ejection fraction is a useful indicator of left ventricular function and can help to diagnose and monitor different CVDs, such as heart failure, and myocardial Measurement of these features can help clinicians diagnose and differentiate between different types of heart disease and determine the appropriate treatment. Moreover, LV and RV volumes and ejection fraction can also provide important prognostic information in cardiovascular disease. For example, reduced LV ejection fraction is a strong predictor of mortality and morbidity in heart failure patients, while increased RV volume and reduced RV ejection fraction are associated with worse outcomes in patients with pulmonary hypertension. Also, it can be used to monitor the efficacy of treatment in cardiovascular disease. For example, improvement in LV ejection fraction following treatment for heart failure is associated with better outcomes, while worsening of RV function despite treatment for pulmonary hypertension may indicate the need for more aggressive therapy [13], [14].

2) RADIOMICS FEATURES

Radiomics computes vast quantities of quantitative information from digital images that are otherwise indistinguishable to the human eye by utilizing a range of sophisticated image processing techniques. These features can distinguish between healthy and diseased tissue by capturing differences in tissue properties. The extracted data can be used to investigate and discover previously unknown correlations between these imaging features and clinical endpoints. Shape and signal intensity-based features are among the radiomics features that are taken from the three-segmented ROIs (LV, RV, and MYO) in both cardiac phases (ED and ES) to detect variations in the forms of each ventricle. The analysis of radiomics features in the myocardium may allow for the identification of tissue-level changes caused by cardiovascular risk factors. Radiomics features were extracted automatically using the open-source Python-based library called Pyradiomics. A total of 684 radiomics features were extracted, with 114 radiomics features per cardiac structure (LV, RV, and MYO) at two different cardiac phases (ES and ED) [35], [36].

a: SIGNAL INTENSITY BASED RADIOMICS FEATURES

Features of signal intensity (SI) may be able to interpret differences in cardiac tissue caused by anomalies brought on by disease processes. Typically, they are divided into two groups: first-order and texture features. The pattern of SI in the ROI is hypothesized to represent underlying tissue features that might point to specific diseases. For example, an irregular arrangement of myofibrils in the myocardium may reflect a heterogeneous SI pattern, which may indicate underlying pathology such as HCM. Radiomics texture analysis aims to identify and characterize different SI patterns in the chosen ROI in a quantitative manner. This is accomplished by using mathematical definitions to describe observed patterns and numerical definitions of the SI inside the segmented volume. The ultimate objective of radiomics modelling is to identify distinctive signal intensity patterns, or radiomics signatures, for significant cardiac diseases. These patterns may be utilized to enhance diagnostic precision or possibly enable automated diagnosis generation in a way that would not be feasible through qualitative inspection of images.

First-order features are statistics based on histograms that describe the global distribution of signal intensities within the specified ROI without taking into account the spatial relationships between them. The global summary of the segmented volume's SI is given by these histogram-based features, but they don't explain how the voxel SIs relate to one another. Different lesions may have first-order parameter values that are similar because of the loss of spatial distribution information.

In contrast, texture radiomic features enable the use of more sophisticated matrix analysis techniques to quantify spatial inter-pixel relationships [24], [25]. Texture features serve to produce the grey values in the images that represent the texture and heterogeneity of the lesions by defining the spatial distribution of voxels. The theory goes that these texture traits might represent traits of the cardiac tissue, which would then represent underlying pathological processes. In this study, each ROI was extracted with 102 first-order features and 474 texture features.

b: RADIOMICS SHAPE FEATURES

Shape characteristics in radiology quantify the 3D size and shape of a segmented volume. Shape features are obtained from an image mask that roughly represents the ROI's

defined edges. Radiomics shape features, which combine more sophisticated geometric quantifiers with traditional shape indices like cavity volumes, may add value to the current CMR indices. Additionally, characteristics are describing the ROI's general geometry (geometrical properties). Furthermore, they may be able to identify patterns of cardiac alterations unique to a given disease that cannot be determined by current CMR indices.

To sum up, quantitative image features that rely on texture or shape have the potential to yield more precise phenotypes and provide deeper spatial information about the lesions than conventional radiological reports. These characteristics may be more accurately used to inform treatment decisions in the future by correlating them with clinical outcomes in addition to clinical data.

C. CLASSICAL FEATURE SELECTION

Feature selection is the process of extracting the relevant features from an input vector based on some criterion. It is also a dimensionality reduction process that can solve the network complexity problem. Furthermore, it is an important step towards improving performance. In ML, various feature selection methods are used. Better feature selection methods result in higher accuracy and a smaller loss function. As a result, it can reduce model training and testing time while also addressing the issue of overfitting. In this study, a Recursive Feature Elimination (RFE) feature selection procedure was used. Reference [38] is utilized to pick up the top best features. RFE fits a Random Forest (RF) ensemble classifier model and removes the weakest feature (or features) based on Gini impurity until the specified number of features is reached. RF feature importance scores are calculated using the Gini importance or mean decrease impurity concept. Gini importance quantifies a feature's total impurity reduction across all decision trees in the RF. Gini impurity quantifies the likelihood of misclassifying a randomly selected element if it were labelled randomly based on the class distribution in the subset. The feature importance is calculated based on the impurity reduction achieved by using that feature. The more an attribute reduces impurity across an ensemble of trees, the more important it is. The number of selected features is limited to only 30 features as the maximum qubits available in NISQ and IBM simulators are 30 qubits.

D. QUANTUM CARDIAC PATHOLOGIES CLASSIFICATION

The proposed model aims to enhance the performance of classical neural network for medical images and to predict cardiac pathologies. The main idea of the proposed model is based on a modified Hardware Efficient Ansatz (MHEA) for efficient use of the resources with improved accuracy. The proposed cardiac pathology classification consists of three parts: first, the encoding part is utilized by using qiskit higher-order angle encoding. Second, the MHEA is proposed as a parameterized model. Finally, the measurement is applied to extract the class labels.

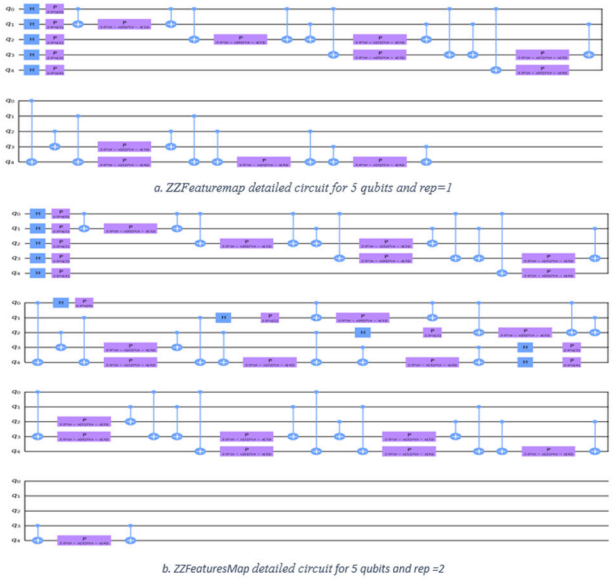

FIGURE 11. ZZFeaturemap detailed circuit for 5 qubits. It consists of a Hadamard gate to let the qubits in a superposition state and a series of Pauli gates with linear entanglement.

1) ENCODE THE CLASSICAL DATA

The goal of a feature map, as mentioned in section II, is to encode the input data for quantum input state preparation (transforming classical data input into the quantum state) to be processed by a quantum algorithm. There are different types of precoded feature maps in Qiskit circuit library. ZZFeaturemap is one of the most powerful precoded feature maps as it involves the application of a series of controlled-Z (CZ) gates to the input data, followed by single-qubit rotations. The CZ gates entangle the qubits and introduce correlations between them, while the single-qubit rotations are used to adjust the amplitudes of the quantum state. ZZFeaturMaps has been selected for data encoding. We varied the depths of these feature maps by depths of 1 and 2 to check the different models' performance. By increasing a feature map's depth, we introduce more entanglement into the model and repeat the encoding circuit. Fig. 11 shows the ZZFeaturemap detailed circuit.

2) APPLY THE PROPOSED MHEA PARAMETERIZED MODEL

HEA is designed to be compatible with near-term quantum hardware so it will be the base for the proposed MHEA. MHEA modifies the well-established HEA to take advantage of its compatibility with NISQ devices while improving its accuracy, speeding it up, and minimizing the number of gates. The goal of the proposed MHEA is to optimize the HEA by removing the rotation around the z-axis. It can improve the circuit's speed, reduce its error rate, reduce computational complexity, improve efficiency, and enable greater configuration flexibility. Also, changing the entanglement property from reverse_linear to linear. Fig 12 shows the difference between the HEA and the proposed Modified version.

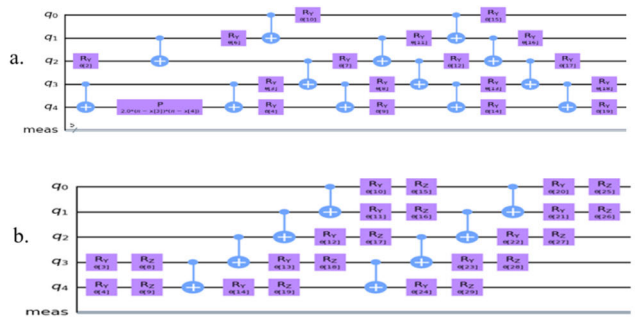

FIGURE 12. Difference between the HEA and the proposed MHEA. In (a) the proposed version of HEA with only Ry gates and linear entanglement while in (b) the original HEA with greater learning parameters as it consists of Ry and Rz gates and inverse linear entanglement structure.

3) MEASUREMENT

The final step is the measurement step, which uses various measurements to estimate the likelihood of belonging to a class. It's the same as taking multiple samples from a distribution of possible computational basis states and calculating an expectation value. Fig. 13 depicts the overall VQC for HQMC-CPC for 5 qubits only for simplicity, but the actual proposed HQMC-CPC consists of 30 qubits.

V. EXPERIMENTAL RESULTS

In this section, we provide the details of the IBM quantum simulators and our experimental scenarios. The entire HQMC-CPC model is implemented on the different simulators provided by Qiskit. The IBM Qiskit [39] quantum computing framework. Hence, we can execute a Python program with quantum operations written using Qiskit package on real-time quantum hardware. The Measurement operation is performed on each wire using qml.exp.PauliZ(n), where n= 1, 2, . . . k is the label of the wire. The model is trained, and the gate parameters are optimized using different optimizers such as Simultaneous Perturbation Stochastic Approximation (SPSA), Constrained Optimization BY Linear Approximations (COBYLA), and Limited-memory Broyden-Fletcher-Goldfarb-Shanno with Bounds (L-BFGS-B). The details of the results of the simulations along with discussions are given in the following sections.

A. SIMULATION

IBM Quantum provides several simulators that can be used to simulate quantum circuits and algorithms. The most commonly used IBM quantum simulators are qasm_simulator, statevector_simulator and unitary_simulator. qasm_simulator simulates the measurement of qubits and provides the results as if they were obtained from a real quantum computer. Additionally, it can simulate up to 32 qubits. Also, statevector_simulator can simulate up to 32 qubits and calculate the exact state of the quantum system at any point during the circuit execution. Moreover, unitary_simulator calculates the exact unitary matrix of the quantum system at any point during the circuit execution.

These simulators can be accessed using the IBM quantum software development kit (SDK) and can be used to develop, test, and debug quantum circuits and algorithms without the need for a physical quantum computer.

Optimization techniques are important in quantum computing because they increase the performance of quantum circuits and algorithms. Parameter optimization is the process of determining the best values for the parameters in a quantum circuit or algorithm. It consists of an objective function that will either be maximized or minimized, as well as certain configurable parameters. This is often accomplished through the use of gradient-free optimization algorithms such as SPSA and COBYLA or using gradient-based optimization algorithms such as (L-BFGS-B).

B. EXPERIMENTAL SETUP AND PERFORMANCE MEASURES

This section uses the ACDC 2017 dataset to conduct experiments aimed at assessing the performance of the proposed HQMC-CPC model. The proposed HQMC-CPC model was developed in Python 3.71. The experiments were performed on a computer with an Intel Core i7-10750H CPU, 32GB RAM, NVIDIA GeForce RTX 2070 GPU, and Windows 10 system. The most common measure for evaluating classification models is the accuracy. The accuracy is computed in terms of TP, TN, FP, and FN. These terms can be defined as follows:

- True Positives (TP): The proposed HQMC-CPC model correctly predicts different cardiac pathology cases and labels each case accurately.
- True Negatives (TN): The proposed HQMC-CPC model correctly predicts different cases and labels them under the negative class.
- False Positive (FP): The proposed HQMC-CPC model incorrectly predicts cardiac pathology cases and labels them as positive.
- False Negatives (FN): The proposed HQMC-CPC model incorrectly predicts different cardiac cases and labels them as negative.

$$Accuracy = \frac{(TP + TN)}{(TP + TN + FP + FN)} \tag{5}$$

C. RESULTS AND DISCUSSION

In this section, the performance of the proposed HQMC-CPC is verified on different simulators with different hyperparameters such as the entanglement structure. The experiment processes involved choosing base models such as Neural Network (NN) and Support Vector Machine (SVM) [40] for initial trials and developing their counterparts using the quantum circuit (QNN) [41] and (QSVM) [42]. Furthermore, the accuracy of the proposed HQMC-CPC has been tested to demonstrate its effectiveness along with a set of well-established ansatzes.

Table 3 depicts different scenarios of different combinations of ansatzes, and different optimizers when tested

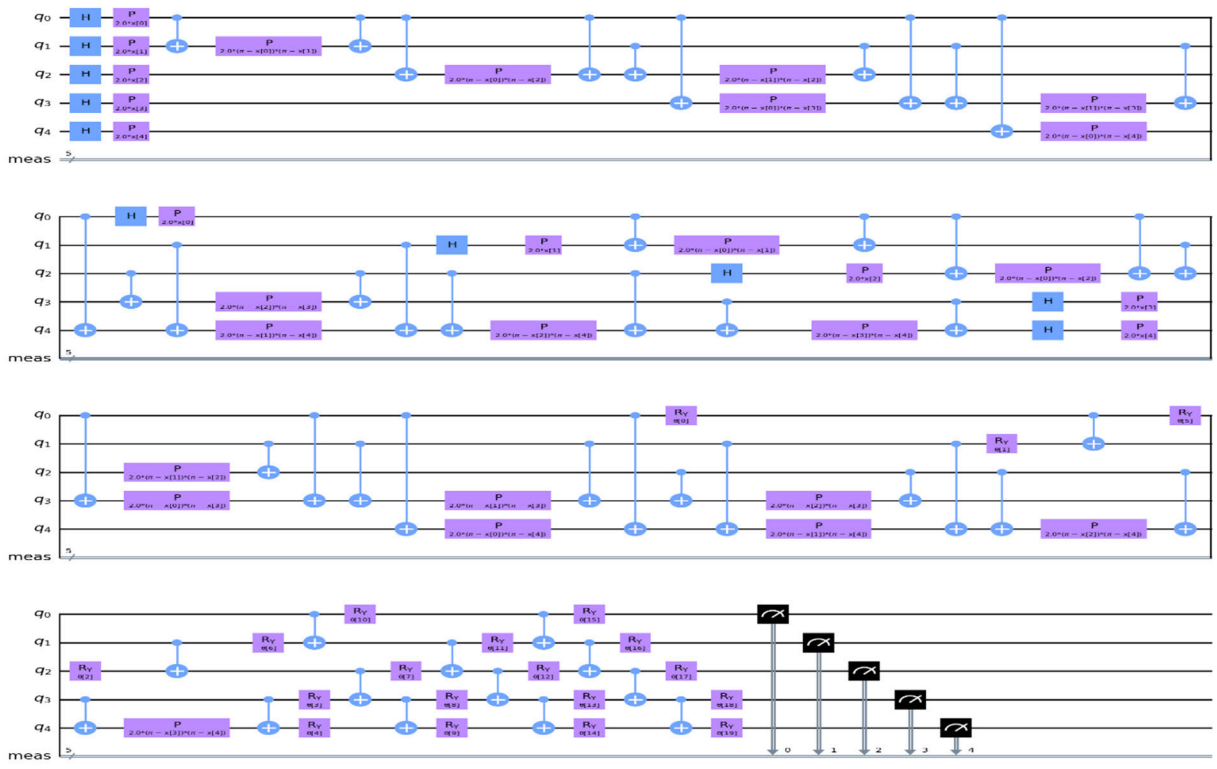

FIGURE 13. Overall VQC for the proposed HQMC-CPC with 5 qubits. It defined as RealAmplitudes(num_qubits=len(X_train[0]), entanglement='linear').

using different simulators. All the scenarios are tested using different numbers of selected features from 5 to 50 features. The evaluation of quantum algorithms is limited to only 30 features as the maximum qubits available in NISQ and IBM simulators is 30 qubits. Tables 4 to 12 illustrate the evaluation of two well-known classical classifiers (NN and SVM) and their counterpart in quantum computing (QNN and QSVM). It also shows the effect of four well-established ansatzes, the variation of different ansatz, and the proposed MHEA. It is worth emphasizing that the results of the proposed HQMC-CPC model are stable and consistent across the different experimental scenarios shown in Table 3. Hence, elucidates the generalization and robustness of the framework.

Table 4 illustrates the evaluation of the SOTA quantum classifiers (QNN and QSVM), their classical version, four well-established Ansatz, and four versions of the proposed model using qasm simulator and applied SPSA optimizer when a different number of features were selected. The results clearly verify the positive impact of the proposed modification on the well-established HEA. As shown in Table 4, the proposed MHEA improved the accuracy of the well-established HEA by 60, NN by 60%, QAOA by 14.28%, VQE by 60%, and QAOAA by 14.28% but the classical SVM and QSVM outperforms MHEA by 75% and 80% respectively when 5 features are selected. Moreover, it shows that the proposed MHEA improved the accuracy

TABLE 3. Scenarios for testing the proposed HQMC-CPC.

Scenario	Optimizer	Simulator
1	SPSA	qasm_simulator
2	SPSA	statevector_simulator
3	SPSA	unitary_simulator
4	COBYLA	qasm_simulator
5	COBYLA	statevector_simulator
6	COBYLA	unitary_simulator
7	L-BFGS-B	qasm_simulator
8	L-BFGS-B	statevector_simulator
9	L-BFGS-B	unitary_simulator

of the well-established HEA by 34.32%, QAOA by 11.11%, VQE by 11.11%, and QAOAA by 21.62% but the classical SVM and NN outperform MHEA by 66.67% and 0.22% respectively and QSVM outperforms the proposed model by 77.77% when 10 features are selected. Also, it shows that the proposed MHEA improved the accuracy of the well-established HEA by 42.85%, QAOA by 11.11%, VQE by 11.11%, and QAOAA by 25%, but the classical SVM and NN outperforms MHEA by 54% and 10% respectively and QSVM outperforms the proposed model by 60% when 15 features are selected. Additionally, it shows that the proposed MHEA improved the accuracy of the well-established

TABLE 4. Evaluation of the state-of-the-art quantum classifiers (QNN and QSVM), their classical version, four well-established ansatz, and the proposed model using qasm simulator and applied SPSA optimizer when a different number of features were selected.

Num of Features	Classical classification		Quantum classification					
				Well-established ansatz				Proposed MHEA
	SVM	NN	QSVM	QAOA	VQE	QAOAA	HEA	
5	0.7	0.25	0.72	0.35	0.25	0.35	0.25	0.4
10	0.75	0.44	0.80	0.40	0.40	0.37	0.33	0.45
15	0.77	0.55	0.80	0.45	0.45	0.40	0.35	0.50
20	0.80	0.69	0.85	0.43	0.35	0.45	0.40	0.65
25	0.82	0.74	0.85	0.48	0.45	0.45	0.55	0.85
30	0.86	0.76	0.90	0.56	0.59	0.58	0.75	0.96
35	0.91	0.83						
40	0.93	0.85						
45	0.93	0.87						
50	0.94	0.93						

TABLE 5. Evaluation of the four well-established Ansatz and the proposed model using statevector_simulator and applied SPSA optimizer when different number of features selected.

Num of Features	Classical classification		Quantum classification					
				Well-established ansatz				Proposed MHEA
	SVM	NN	QSVM	QAOA	VQE	QAOAA	HEA	
5	0.7	0.25	0.72	0.4	0.3	0.2	0.25	0.3
10	0.75	0.449	0.8	0.45	0.40	0.2	0.35	0.35
15	0.77	0.55	0.8	0.45	0.45	0.4	0.45	0.50
20	0.80	0.69	0.85	0.58	0.55	0.45	0.65	0.65
25	0.82	0.74	0.85	0.62	0.66	0.55	0.79	0.78
30	0.86	0.76	0.9	0.65	0.61	0.63	0.96	0.96
35	0.91	0.83						
40	0.93	0.85						
45	0.935	0.87						
50	0.94	0.93						

HEA by 62.5%, QAOA by 51.11%, VQE by 85.71%, and QAOAA by 44.44% but the classical SVM and QSVM outperforms MHEA by 23.07% and 30.76% respectively when 20 features are selected. Moreover, when 25 features are selected the proposed MHEA shows equivalent accuracy to QSVM while it outperforms all the other models. Finally, when 30 features are selected the proposed MHEA shows superior improvement over all the other models. It improved the accuracy of the well-established HEA by 28%, QSVM by 6.667%, QAOA by 70.41%, VQE by 62.71%, and QAOAA by 65.51% and the classical SVM and NN by 11.62% and 26.31% respectively. It is worth noting that the proposed MHEA with only 30 features outperforms the classical SVM and NN by 2.12% and 3.125% respectively when 50 features are selected. Moreover, the time complexity of the classical models when 50 features are selected is around three times the proposed model with 30 features with limited accuracy.

Table 5 illustrates the evaluation of the state-of-the-art quantum classifiers (QNN and QSVM), their classical version, four well-established Ansatz, and four versions of the proposed model using a statevector simulator and applied SPSA optimizer when a different number of features were selected. The results clearly verify the positive impact of the of the proposed modification on the well-established HEA. As shown in Table 5, the proposed MHEA improved the accuracy of the well-established HEA and classical NN by 20%, and QAOAA by 50% while having the same accuracy as VQE. While the classical SVM and QSVM outperform MHEA when 5 features are selected. Moreover, it shows that the proposed MHEA has the same accuracy as the well-established HEA but the classical models, QSVM outperforms MHEA when 10 and 15 features are selected. When 20 features are selected the proposed MHEA draws an equivalent accuracy as the HEA and it improves the accuracy of QAOA, VQE and QAOAA. Additionally, it shows that the proposed MHEA improved the accuracy of all the listed models except the HEA and QSVM when 25 features were selected. Moreover, when 25 features, are selected the proposed MHEA shows equivalent accuracy like QSVM while it outperforms all the other models. Finally when 30 features are selected the proposed MHEA shows superior improvement over all the other models except HEA it has the same accuracy. It improved the accuracy of the QSVM by 6.667%, QAOA by 47.69%, VQE by 57.73%, and QAOAA by 52.38% and the classical SVM and NN by 11.62% and 26.31% respectively. It is worth noting that the proposed MHEA with only 30 features outperforms the classical SVM and NN by 2.12% and 3.125% respectively when 50 features are selected.

Table 6 illustrates the evaluation of the SOTA quantum classifiers (QNN and QSVM), their classical version, four well-established Ansatz, and four versions of the proposed

TABLE 6. Evaluation of the state-of-the-art quantum classifiers (QNN and QSVM), their classical version, four well-established Ansatz, and the proposed model using unitary simulator and applied SPSA optimizer applied when different number of features selected.

Num of Features	Classical classification		Quantum classification					
				Well-established ansatz				
	SVM	NN	QSVM	QAOA	VQE	QAOAA	HEA	Proposed MHEA
5	0.7	0.25	0.72	0.4	0.25	0.35	0.35	0.4
10	0.75	0.449	0.8	0.45	0.40	0.40	0.45	0.45
15	0.77	0.55	0.8	0.53	0.52	0.60	0.58	0.60
20	0.80	0.69	0.85	0.65	0.65	0.65	0.70	0.78
25	0.82	0.74	0.85	0.74	0.61	0.75	0.84	0.85
30	0.86	0.76	0.9	0.81	0.79	0.84	0.92	0.97
35	0.91	0.83						
40	0.93	0.85						
45	0.935	0.87						
50	0.94	0.93						

TABLE 7. Evaluation of the state-of-the-art quantum classifiers (QNN and QSVM), their classical version, four well-established Ansatz, and the proposed model using qasm simulator and applied COBYLA optimizer when different number of features selected.

Num of Features	Classical classification		Quantum classification					
				Well-established ansatz				
	SVM	NN	QSVM	QAOA	VQE	QAOAA	HEA	Proposed MHEA
5	0.7	0.25	0.72	0.40	0.35	0.35	0.35	0.4
10	0.75	0.449	0.8	0.40	0.40	0.45	0.47	0.45
15	0.77	0.55	0.8	0.45	0.45	0.45	0.55	0.50
20	0.80	0.69	0.85	0.59	0.65	0.60	0.62	0.65
25	0.82	0.74	0.85	0.76	0.70	0.74	0.73	0.85
30	0.86	0.76	0.9	0.85	0.82	0.85	0.88	0.96
35	0.91	0.83						
40	0.93	0.85						
45	0.935	0.87						
50	0.94	0.93						

model using a unitary simulator and applied SPSA optimizer when a different number of features were selected. The results clearly verify the positive impact of the of the proposed modification on the well-established HEA. As shown in Table 6, the proposed MHEA improved the accuracy of the well-established HEA and QAOAA by 14.28%, and 60% over VQE and NN while having the same accuracy as QAOA. While the classical SVM and QSVM outperform MHEA when 5 features are selected. Moreover, it shows that the proposed MHEA has the same accuracy as the well-established HEA, QAOA, and NN but the SVM, QSVM outperform MHEA when 10 features are selected. When 20 features are selected the proposed MHEA improves the accuracy of all the listed quantum models except QSVM.

Additionally, it shows that the proposed MHEA has the same accuracy as QSVM and improved the accuracy of all other listed models when 25 features were selected. Finally, when 30 features are selected the proposed MHEA shows superior improvement over all the other models. It improved the accuracy of the QSVM by 7.77 %, QAOA by 19.75%, VQE by 22.78%, QAOAA by 15.47%, and the classical SVM and NN by 12.79% and 27.63% respectively. It is worth noting that the proposed MHEA with only 30 features outperforms the classical SVM and NN by 3.19% and 4.3% respectively when 50 features are selected.

Table 7 illustrates the evaluation of the SOTA quantum classifiers (QNN and QSVM), their classical version, four well-established Ansatz, and four versions of the proposed model using a qasm simulator and applied COBYLA optimizer when a different number of features were selected. The results verify the positive impact of the proposed modification on the well-established HEA. As shown in Table 7, the proposed MHEA improved the accuracy of the well-established HEA by 14.28% when 5 features were selected. Moreover, it shows that the HEA outperforms the proposed MHEA by 4.44% and 10% when 10 and 15 features are selected. When 20 features are selected the proposed MHEA improves the accuracy of all the listed quantum models except QSVM. Additionally, it shows that the proposed MHEA has the same accuracy as QSVM and improved the accuracy of all other listed models when 25 features were selected. Finally, when 30 features are selected the proposed MHEA shows superior improvement over all the other models. It improved the accuracy of the QSVM by 6.66 %, QAOA by 12.94%, VQE by 17.07%, QAOAA by 29.41% and the classical SVM and NN by 11.62% and 27.63% respectively. It is worth noting that the proposed MHEA with only 30 features outperforms the classical SVM and NN by 2.12% and 3.125% respectively when 50 features are selected.

Table 8 illustrates the evaluation of the SOTA quantum classifiers (QNN and QSVM), their classical version, four

TABLE 8. Evaluation of the four well-established Ansatz and the proposed model using statevector_simulator and applied COBYLA optimizer applied when different number of features selected.

Num of Features	Classical classification		Quantum classification					
				Well-established ansatz				Proposed MHEA
	SVM	NN	QSVM	QAOA	VQE	QAOAA	HEA	
5	0.7	0.25	0.72	0.4	0.3	0.40	0.45	0.40
10	0.75	0.449	0.8	0.45	0.39	0.52	0.49	0.47
15	0.77	0.55	0.8	0.51	0.45	0.61	0.55	0.58
20	0.80	0.69	0.85	0.59	0.55	0.65	0.65	0.72
25	0.82	0.74	0.85	0.65	0.66	0.75	0.79	0.86
30	0.86	0.76	0.9	0.75	0.81	0.83	0.95	0.95
35	0.91	0.83						
40	0.93	0.85						
45	0.935	0.87						
50	0.94	0.93						

TABLE 9. Evaluation of the state-of-the-art quantum classifiers (QNN and QSVM), their classical version, four well-established Ansatz, and the proposed model using the unitary simulator and COBYLA optimizer applied when a different number of features were selected.

Num of Features	Classical classification		Quantum classification					
				Well-established ansatz				Proposed MHEA
	SVM	NN	QSVM	QAOA	VQE	QAOAA	HEA	
5	0.7	0.25	0.72	0.42	0.25	0.35	0.35	0.4
10	0.75	0.449	0.8	0.54	0.40	0.47	0.45	0.51
15	0.77	0.55	0.8	0.63	0.45	0.54	0.59	0.68
20	0.80	0.69	0.85	0.71	0.64	0.65	0.68	0.75
25	0.82	0.74	0.85	0.75	0.73	0.72	0.72	0.86
30	0.86	0.76	0.9	0.81	0.82	0.86	0.91	0.97
35	0.91	0.83						
40	0.93	0.85						
45	0.935	0.87						
50	0.94	0.93						

well-established Ansatz, and four versions of the proposed model using a statevector simulator and applied COBYLA optimizer when a different number of features were selected. The results clearly verify the advantages of the proposed modification on the well-established HEA. As shown in Table 8, the HEA outperforms the proposed MHEA by 12.5% and 4.25% when 5 and 10 features are selected respectively.

When 15 and 20 features are selected the proposed MHEA improves the accuracy of all the listed quantum models except QSVM. Additionally, it shows that the proposed MHEA improved the accuracy of all listed models when 25 features were selected. Finally, when 30 features are selected the proposed MHEA has an equivalent accuracy as HEA and superior improvement over all the other models. It improved the accuracy of the QSVM by 6.66 %, QAOA by 14.45%, VQE by 17.28%, QAOAA by 12.04%, and the classical SVM and NN by 10.46% and 25% respectively. It is worth noting that the proposed MHEA with only 30 features outperforms the classical SVM and NN by 1.06% and 2.15% respectively.

Table 9 illustrates the evaluation of the SOTA quantum classifiers (QNN and QSVM), their classical version, four well-established Ansatz, and four versions of the proposed model using a unitary simulator and applied COBYLA optimizer when a different number of features were selected. The results clearly verify the effectiveness of the proposed modification on the well-established HEA. As shown in Table 9, the proposed MHEA outperforms HEA, VQE, and QAOAA for all number of extracted features. Moreover, the proposed MHEA outperforms QAOA for all numbers of extracted features except when 10 features are selected. Finally, when 30 features are selected the proposed MHEA has an equivalent accuracy as HEA and superior improvement over all the other models. It improved the accuracy of the QSVM by 7.77%, QAOA by 19.75%, VQE by 18.29%, QAOAA by 12.79%, and the classical SVM and NN by 12.79% and 27.63% respectively. It is worth noting that the proposed MHEA with only 30 features outperforms the classical SVM and NN by 3.19% and 4.3% respectively when 50 features are selected.

Table 10 illustrates the evaluation of the SOTA quantum classifiers (QNN and QSVM), their classical version, four well-established Ansatz, and four versions of the proposed model using a qasm simulator and L-BFGS-B optimizer when a different number of features were selected. The results clearly verify the positive effect of the proposed modification on the well-established HEA. As shown in Table 10, the proposed MHEA outperforms HEA, VQE, and QAOAA for all numbers of extracted features. Moreover, the proposed MHEA outperforms QAOA for all numbers of extracted features except when 15 features are selected both have the same accuracy. Finally, when 30 features are selected the

TABLE 10. Evaluation of the state-of-the-art quantum classifiers (QNN and QSVM), their classical version, four well-established Ansatz, and the proposed model using qasm simulator and L-BFGS-B optimizer applied when different number of features selected.

Num of Features	Classical classification		Quantum classification					
				Well-established ansatz				
	SVM	NN	QSVM	QAOA	VQE	QAOAA	HEA	Proposed MHEA
5	0.7	0.25	0.72	0.5	0.25	0.35	0.35	0.4
10	0.75	0.449	0.8	0.54	0.40	0.4	0.41	0.45
15	0.77	0.55	0.8	0.58	0.45	0.49	0.55	0.58
20	0.80	0.69	0.85	0.62	0.56	0.59	0.64	0.69
25	0.82	0.74	0.85	0.71	0.73	0.72	0.85	0.87
30	0.86	0.76	0.9	0.85	0.82	0.80	0.95	0.96
35	0.91	0.83						
40	0.93	0.85						
45	0.935	0.87						
50	0.94	0.93						

TABLE 11. Evaluation of the four well-established Ansatz the proposed model using statevector_simulator and QAOA-P optimizer applied when different number of features selected.

Num of Features	Classical classification		Quantum classification					
				Well-established ansatz				Proposed MHEA
	SVM	NN	QSVM	QAOA	VQE	QAOAA	HEA	
5	0.7	0.25	0.72	0.40	0.31	0.30	0.45	0.37
10	0.75	0.449	0.8	0.53	0.42	0.38	0.51	0.42
15	0.77	0.55	0.8	0.62	0.56	0.42	0.55	0.50
20	0.80	0.69	0.85	0.73	0.69	0.65	0.65	0.65
25	0.82	0.74	0.86	0.81	0.76	0.82	0.79	0.78
30	0.86	0.76	0.9	0.89	0.91	0.93	0.95	0.95
35	0.91	0.83						
40	0.93	0.85						
45	0.935	0.87						
50	0.94	0.93						

proposed MHEA has an equivalent accuracy as HEA and superior improvement over all the list models. It improves the accuracy of the QSVM by 6.66%, QAOA by 12.94%, VQE by 17.07%, QAOAA by 20%, and the classical SVM and NN by 11.62% and 26.31% respectively. It is worth noting that the proposed MHEA with only 30 features outperforms the classical SVM and NN by 3.19% and 4.3% respectively when 50 features are selected.

Table 11 illustrates the evaluation of the SOTA quantum classifiers (QNN and QSVM), their classical version, four well-established Ansatz, and four versions of the proposed model using a statevector simulator and L-BFGS-B optimizer when a different number of features were selected. The results clearly verify the positive impact of the proposed modification on the well-established HEA. As shown in Table 11, the HEA outperforms the proposed MHEA when 5,10, and 15 features are extracted. Moreover, the proposed MHEA has the same accuracy as HEA when 20 features are selected. Finally, when 30 features are selected the proposed MHEA has an equivalent accuracy as HEA and superior improvement over all the list models. It improves the accuracy of the QSVM by 5.26%, QAOA by 25%, VQE by 4.39%, QAOAA by 2.15%, and the classical SVM and NN by 10.46% and 25% respectively. It is worth noting that the proposed MHEA with only 30 features outperforms the classical SVM and NN by 1.06 % and 2.15 % respectively when 50 features are selected.

Table 12 illustrates the evaluation of the SOTA quantum classifiers (QNN and QSVM), their classical version, four well-established Ansatz, and four versions of the proposed model using a unitary simulator and L-BFGS-B optimizer when a different number of features were selected. The results clearly verify the positive impact of the proposed modification on the well-established HEA. As shown in Table 12, the proposed MHEA outperforms HEA, VQE, QAOA, and QAOAA for all numbers of extracted features. Moreover, when 30 features are selected the proposed MHEA has an equivalent accuracy as HEA and superior improvement over all the list models. It improves the accuracy of the QSVM and QAOA by 6.66%, VQE by 7.86%, QAOAA by 2.12%, and the classical SVM and NN by 11.62% and 26.31% respectively. It is worth noting that the proposed MHEA with only 30 features outperforms the classical SVM and NN by 3.19% and 4.3% respectively when 50 features are selected.

Fig. 14 shows the training and validation learning curves using the MHEA when the parameters are optimized using SPSA optimizer and tested using a unitary simulator. It indicates that the training and validation stages of the proposed model follow a similar trend, and the minimal performance difference reduces the risk of overfitting.

The evaluation of the proposed MHEA in terms of average accuracy across different scenarios when different

TABLE 12. Evaluation of the state-of-the-art quantum classifiers (QNN and QSVM), their classical version, four well-established Ansatz, and the proposed model using a unitary simulator and applied L-BFGS-B optimizer applied when different number of features selected.

Num of Features	Classical classification		Quantum classification					
				Well-established ansatz				
	SVM	NN	QSVM	QAOA	VQE	QAOAA	HEA	Proposed MHEA
5	0.7	0.25	0.72	0.41	0.25	0.35	0.35	0.4
10	0.75	0.449	0.8	0.45	0.40	0.45	0.48	0.51
15	0.77	0.55	0.8	0.53	0.49	0.57	0.60	0.63
20	0.80	0.69	0.85	0.63	0.64	0.68	0.71	0.78
25	0.82	0.74	0.86	0.71	0.73	0.79	0.82	0.85
30	0.86	0.76	0.9	0.90	0.89	0.94	0.95	0.96
35	0.91	0.83						
40	0.93	0.85						
45	0.935	0.87						
50	0.94	0.93						

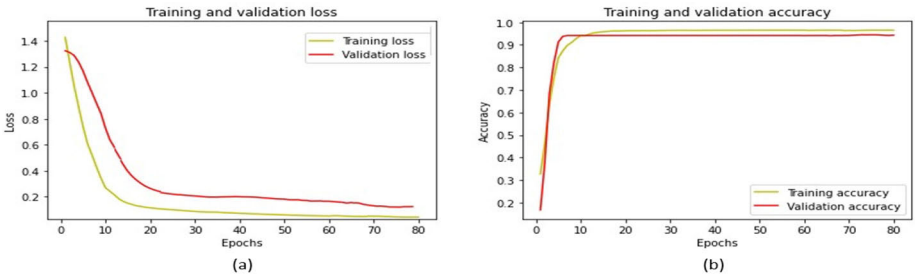

FIGURE 14. HQMC-CPC accuracy (a) and losses (b) during the training and validation process of multi-class cardiac pathologies classification.

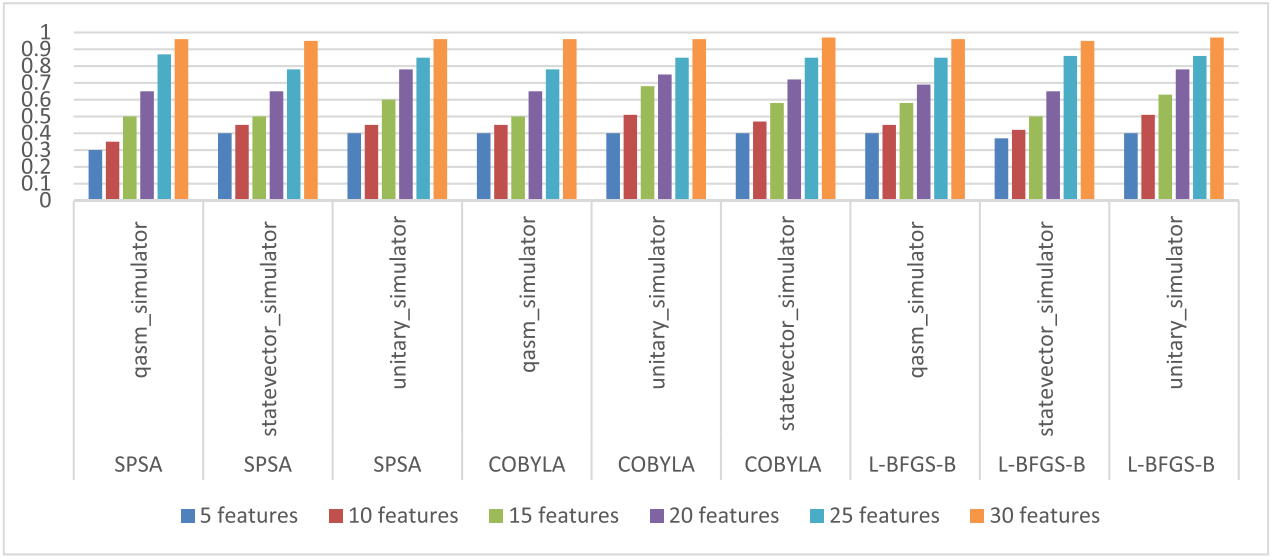

FIGURE 15. Evaluation of the proposed MHEA in terms of average accuracy across different scenarios when different optimizers, different simulators, and different numbers of features are used.

optimizers, different simulators, and different numbers of features are used is depicted in Fig 15. Also, Fig 16 depicts the evaluation of the proposed MHEA in terms of average testing time across different scenarios when different optimizers, different simulators, and different numbers of features are used. It shows the robustness of the proposed MHEA as by changing the optimizer and simulator, the change in the results is very small. For 30 features, the average accuracy value is 96± 0.007 and the testing time is around 53 sec. Moreover, it shows the maximum accuracy achieved when SPSA and COBYLA optimizers are tested using unitary simulator and 30 features are selected. In addition, the variation of time is very small compared to the improved accuracy.

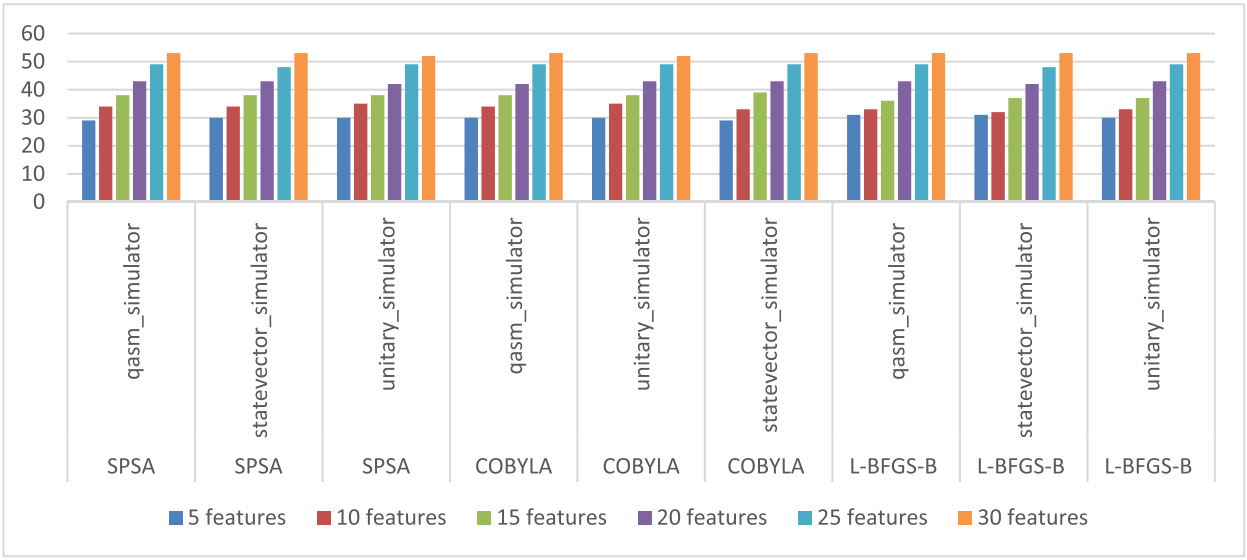

FIGURE 16. Evaluation of the proposed MHEA in terms of average testing time across different scenarios when different optimizers, different simulators, and different numbers of features are used.

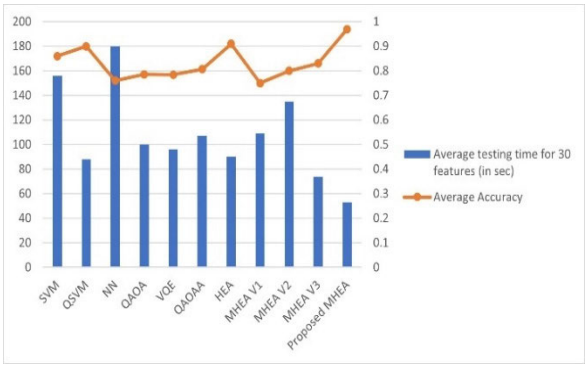

FIGURE 17. Average testing time and accuracy for different classification approaches including classical and quantum classifiers.

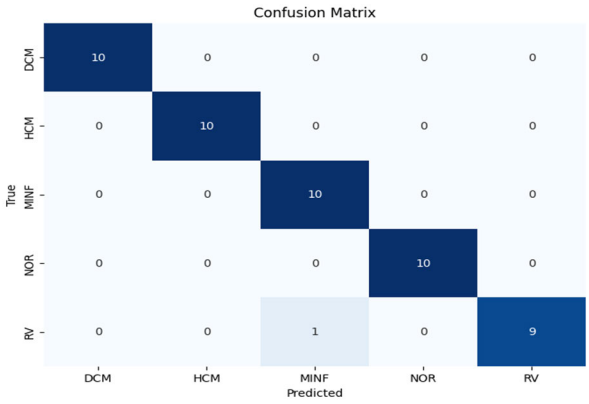

FIGURE 18. Confusion Matrix of Scenario 3 and 6 when selecting 30 features and SPSA and COBYLA optimizers are tested using unitary simulator.

Testing time is another aspect to demonstrate the overall effectiveness of the proposed HQMC-CPC model. Fig. 17

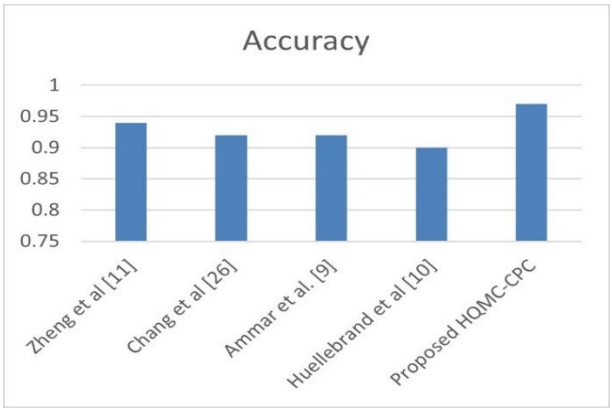

FIGURE 19. Comparison with state-of-the-art cardiac pathologies classification methods on the ACDC dataset.

shows the analysis of classification for the nine scenarios in terms of average accuracy, and testing time. It shows that the proposed HQMC-CPC model achieves the highest average accuracy and lowest average testing time compared to the other classification methods listed. Moreover, it depicts that the average testing time for the proposed model HQMC-CPC takes less than one-third of the classical classifiers. Also, it minimizes the testing time of the well-established HEA by around 40% by minimizing the rotation gates as mentioned above.

Fig. 18 illustrates the confusion matrix of the confusion matrix of the proposed HQMC-CPC for the best two scenarios when SPSA and COBYLA optimizers are tested using unitary simulator and 30 features are selected. It depicts that the proposed HQMC-CPC is able to classify DCM, HCM and NOR accurately with f-score equals to 1, while in calculating f-score for MINF and RV are 0.95 and 0.94 respectively.

TABLE 13. Evaluation of the deep learning models, and the proposed HQMC-CPC classifier in terms of classification accuracy and testing time where end-to-end learning or handcrafted features fed to classifer and input MRI original or segmented.

Model	Feature extraction		Input MRI		Performance measures	
	Handcrafted Features	Deep learning features	Original MRI	Segmented MRI	Accuracy	Testing Time
ResNet50[43]		✓	✓		0.64	172
		✓		✓	0.88	84
ResNet101[43]		✓	✓		0.68	196
		✓		✓	0.91	100
HQMC-CPC		✓	✓		0.85	76
		✓		✓	0.92	62
	✓			✓	**0.97**	**53**

TABLE 14. Evaluation of different varations of well-established HEA by modifying the entanglement type or quantum gates or number of circuit repition in terms of accuracy and testing time.

VQC variations	Entanglement types			Quantum Gates				Performance measures	
	Full	Linear	Reverse-linear	Ry	Rz	CNOT	Rep	Accuracy	Testing Time in sec
HEA			✓	✓	✓	✓	1	0.91	90
MHEA V1			✓	✓	✓	✓	2	0.75	109
MHEA V2	✓			✓	✓	✓	1	0.80	135
MHEA V3		✓		✓	✓	✓	1	0.83	74
MHEA		✓		✓		✓	1	**0.97**	**53**

The performance of HQMC-CPC is compared to existing approaches on the ACDC 2017 dataset for further validation. The comparison between the results for cardiac pathology classification on ACDC 2017 dataset is shown in Fig. 19. HQMC-CPC significantly outperformed all other methods in terms of the accuracy on the ACDC test dataset. The proposed HQMC-CPC outperforms Huang et al [11] in terms of accuracy by 3.19%. In addition, their model is semi supervised as they use ApparentFlow-net for motion feature extraction and then select the top features manually. The proposed model outperforms Chang and Jung [16] and Ammar et al. [12] by 5.43%. The proposed HQMC-CPC is able to classify the different cardiac pathologies with an average minimum performance gap of 3.19%. While the average maximum improvement in cardiac pathologies classification is 7.77%.

D. ABLATION STUDY AND ANALYSIS

Another experiment is conducted with two-fold objectives. The first objective is to contrast the performance of quantum circuits versus deep learning models using features extracted from deep learning network. The second objective is to signify the impact of handcrafted (radiomics and clinical) features versus deep learning features by applying the proposed quantum circuit on both. Firstly, table 11 demonstrates the effectiveness of the proposed HQCM-CPC over ResNet50 and ResNet101 models when the original MRI or the segment biventricular MRI is input to the deep end-to-end deep learning model. The proposed HQMC-CPC outperforms ResNet50 in case it takes the original MRI or the segmented biventricular MRI as input by 32% and 4% respectively using the same set of features extracted from ResNet50. Also, when using the same set of features extracted from ResNet101 the performance gap between the proposed HQMC-CPC and ResNet101 is 25% And 1% in case of input the original MRI or the segmented biventricular MRI respectively. Furthermore, It can be seen from table 13 that the proposed HQMC-CPC is the fastest model for CVDs diagnosis, and it outperforms the other four deep-learning approaches. Moreover, In case of input the segmented biventricular MRI to the ResNet101, the testing time of ResNet101 model is almost double the testing time of the proposed model. Secondly, it is worth noting that the usage of handcrafted features by combining clinical and radiomics features outperforms the deep learning features [13], [14]. As shown in table 11, while the usage of features extracted by the deep learning approaches and classifying these features using the proposed quantum circuit outperforms the end-to-end deep learning approaches, the proposed HQMC-CPC based on the fusion of radiomics, and clinical handcrafted features outperform all the other versions by minimum improvement by 5.4% and decrease the testing time by 14%.

Another ablation experiment shown in table 14 verifies the effectiveness of the proposed MHEA VQC. The ablation study includes three main parameters including entanglement type, quantum gates, and repetition of the quantum circuit. A set of experiments is conducted to validate the proposed modification that has been applied to the proposed MHEA by comparing it with the original well-established HEA and three variations of it by changing the repetition parameter to two as in MHEA V1 to introduce more entanglement into the VQC and repeating the quantum circuit. This modification does not improve the accuracy of the well-established HEA and it increases the testing time by 20% so repetition parameters have been kept equal to one and there is no need to repeat the circuit. In addition, we also investigate the importance of the entanglement type by changing it to full and linear in MHEA V2 and MHEA V3 respectively. It is worth noting that linear entanglement in MHEA V3 improves

the time by around 21% while the accuracy has decreased. Finally, in the proposed version of HEA (MHEA) keep the repetition parameter equal to one change the entanglement type to linear as in MHEA V3 and remove the rotation gates around the z-axis which minimizes the learning parameters improves the accuracy by 6.5% and decreases the testing time by around 31%.

VI. CONCLUSION

Quantum computing offers promising prospects for handling extremely complicated data processing problems that are currently unsolvable with conventional computing techniques. Quantum computers can effectively handle the vast volumes of data that are available today with high performance. In this paper, we extracted a large set of discriminative features consisting of radiomics and clinical features. The feature set is considerably reduced through recursive feature selection to obtain 30 features. Moreover, we designed a hybrid quantum multiclass cardiac pathologies classification (HQMC-CPC) model by modifying the well-established HEA. The results obtained from experiments conducted on different IBM simulators show that the proposed MHEA is compatible with the real quantum hardware. Alternatively, our approach can classify multiple classes considering the availability of qubits in NISQ. This is supported by the evaluation of the ACDC 2017 test dataset which obtained a classification accuracy of 97%, where the proposed method achieves higher performance compared to SOTA approaches in classification. HQMC-CPC achieved an average maximum improvement in classification by 7.77%. Moreover, it is worth noting that the average testing time of the proposed HQMCCPC model is less than one-third of the classical classifiers. Also, it minimizes the testing time of the well-established HEA by around 40%. In conclusion, HQMC-CPC aids in early diagnosis and therapy planning of cardiovascular diseases, improving prognosis. More research can be done to improve existing algorithms or to develop new machine learning algorithms for different medical image analysis that can be implemented on a quantum computer.

REFERENCES

[1] *Cardiovascular Diseases (CVDs)*. Accessed: Sep. 22, 2023. [Online]. Available: https://www.who.int/news-room/fact-sheets/detail/cardiovascular-diseases-(cvds)

[2] A. Atehortúa, E. Romero, and M. Garreau, "Characterization of motion patterns by a spatio-temporal saliency descriptor in cardiac cine MRI," *Comput. Methods Programs Biomed.*, vol. 218, May 2022, Art. no. 106714, doi: 10.1016/j.cmpb.2022.106714.

[3] X. Shi and C. Li, "Anatomical knowledge based level set segmentation of cardiac ventricles from MRI," *Magn. Reson. Imag.*, vol. 86, pp. 135–148, Feb. 2022, doi: 10.1016/j.mri.2021.10.005.

[4] Q. Tong, C. Li, W. Si, X. Liao, Y. Tong, Z. Yuan, and P. A. Heng, "RIANet: Recurrent interleaved attention network for cardiac MRI segmentation," *Comput. Biol. Med.*, vol. 109, pp. 290–302, Jun. 2019, doi: 10.1016/j.compbiomed.2019.04.042.

[5] S. Batool, I. A. Taj, and M. Ghafoor, "Ejection fraction estimation from echocardiograms using optimal left ventricle feature extraction based on clinical methods," *Diagnostics*, vol. 13, no. 13, p. 2155, Jun. 2023, doi: 10.3390/diagnostics13132155.

[6] S. Hatipoglu, R. H. Mohiaddin, P. Gatehouse, F. Alpendurada, A. J. Baksi, C. Izgi, S. K. Prasad, D. J. Pennell, and S. Krupickova, "Performance of artificial intelligence for biventricular cardiovascular magnetic resonance volumetric analysis in the clinical setting," *Int. J. Cardiovascular Imag.*, vol. 38, no. 11, pp. 2413–2424, Jun. 2022, doi: 10.1007/s10554-022-02649-1.

[7] A. Varela and C. H. Davos, "Cardiovascular anatomy and physiology: Basic principles and challenges," in *Cardiovascular Computing–Methodologies and Clinical Applications*. Singapore: Springer, 2019, pp. 3–11, doi: 10.1007/978-981-10-5092-3_1.

[8] S. Whiteman, Y. Alimi, M. Carrasco, J. Gielecki, A. Zurada, and M. Loukas, "Anatomy of the cardiac chambers: A review of the left ventricle," *Transl. Res. Anatomy*, vol. 23, Jun. 2021, Art. no. 100095, doi: 10.1016/j.tria.2020.100095.

[9] P. Huang, X. Tan, X. Zhou, S. Liu, F. Mercaldo, and A. Santone, "FABNet: Fusion attention block and transfer learning for laryngeal cancer tumor grading in P63 IHC histopathology images," *IEEE J. Biomed. Health Informat.*, vol. 26, no. 4, pp. 1696–1707, Apr. 2022, doi: 10.1109/JBHI.2021.3108999.

[10] P. Huang, X. Zhou, P. He, P. Feng, S. Tian, Y. Sun, F. Mercaldo, A. Santone, J. Qin, and H. Xiao, "Interpretable laryngeal tumor grading of histopathological images via depth domain adaptive network with integration gradient CAM and priori experience-guided attention," *Comput. Biol. Med.*, vol. 154, Mar. 2023, Art. no. 106447, doi: 10.1016/j.compbiomed.2022.106447.

[11] P. Huang, P. He, S. Tian, M. Ma, P. Feng, H. Xiao, F. Mercaldo, A. Santone, and J. Qin, "A ViT-AMC network with adaptive model fusion and multiobjective optimization for interpretable laryngeal tumor grading from histopathological images," *IEEE Trans. Med. Imag.*, vol. 42, no. 1, pp. 15–28, Jan. 2023, doi: 10.1109/TMI.2022.3202248.

[12] A. Ammar, O. Bouattane, and M. Youssfi, "Automatic cardiac cine MRI segmentation and heart disease classification," *Computerized Med. Imag. Graph.*, vol. 88, Mar. 2021, Art. no. 101864, doi: 10.1016/j.compmedimag.2021.101864.

[13] M. Huellebrand, M. Ivantsits, L. Tautz, S. Kelle, and A. Hennemuth, "A collaborative approach for the development and application of machine learning solutions for CMR-based cardiac disease classification," *Frontiers Cardiovascular Med.*, vol. 9, Mar. 2022, Art. no. 829512, doi: 10.3389/fcvm.2022.829512.

[14] Q. Zheng, H. Delingette, and N. Ayache, "Explainable cardiac pathology classification on cine MRI with motion characterization by semi-supervised learning of apparent flow," *Med. Image Anal.*, vol. 56, pp. 80–95, Aug. 2019, doi: 10.1016/j.media.2019.06.001.

[15] F. Li, W. Li, X. Gao, R. Liu, and B. Xiao, "DCNet: Diversity convolutional network for ventricle segmentation on short-axis cardiac magnetic resonance images," *Knowl.-Based Syst.*, vol. 258, Dec. 2022, Art. no. 110033, doi: 10.1016/j.knosys.2022.110033.

[16] Y. Chang and C. Jung, "Automatic cardiac MRI segmentation and permutation-invariant pathology classification using deep neural networks and point clouds," *Neurocomputing*, vol. 418, pp. 270–279, Dec. 2020, doi: 10.1016/j.neucom.2020.08.030.

[17] J. Xiao, Y. Li, Y. Tian, D. Xu, P. Li, S. Zhao, and Y. Pan, "Visual recognition of cardiac pathology based on 3D parametric model reconstruction," *Frontiers Inf. Technol. Electron. Eng.*, vol. 23, no. 9, pp. 1324–1337, Sep. 2022, doi: 10.1631/fitee.2200102.

[18] J. D. Martín-Guerrero and L. Lamata, "Quantum machine learning: A tutorial," *Neurocomputing*, vol. 470, pp. 457–461, Jan. 2022, doi: 10.1016/j.neucom.2021.02.102.

[19] M. Cerezo, G. Verdon, H.-Y. Huang, L. Cincio, and P. J. Coles, "Challenges and opportunities in quantum machine learning," *Nature Comput. Sci.*, vol. 2, no. 9, pp. 567–576, Sep. 2022, doi: 10.1038/s43588-022-00311-3.

[20] G. N. Balaji, T. S. Subashini, and N. Chidambaram, "Detection and diagnosis of dilated cardiomyopathy and hypertrophic cardiomyopathy using image processing techniques," *Eng. Sci. Technol., Int. J.*, vol. 19, no. 4, pp. 1871–1880, Dec. 2016, doi: 10.1016/j.jestch.2016.10.001.

[21] M. A. Nielsen and I. L. Chuang, *Quantum Computation and Quantum Information: 10th Anniversary Edition*. Cambridge, U.K.: Cambridge Univ. Press, 2011.

[22] D. Konar, S. Bhattacharyya, T. K. Gandhi, and B. K. Panigrahi, "A quantum-inspired self-supervised network model for automatic segmentation of brain MR images," *Appl. Soft Comput.*, vol. 93, Aug. 2020, Art. no. 106348, doi: 10.1016/j.asoc.2020.106348.

[23] F. Jazaeri, A. Beckers, A. Tajalli, and J.-M. Sallese, "A review on quantum computing: Qubits, cryogenic electronics and cryogenic MOSFET physics," 2019, *arXiv:1908.02656*.
[24] S. S. Gill, A. Kumar, H. Singh, M. Singh, K. Kaur, M. Usman, and R. Buyya, "Quantum computing: A taxonomy, systematic review and future directions," *Softw., Pract. Exper.*, vol. 52, no. 1, pp. 66–114, Jan. 2022, doi: 10.1002/spe.3039.
[25] L. Wei, H. Liu, J. Xu, L. Shi, Z. Shan, B. Zhao, and Y. Gao, "Quantum machine learning in medical image analysis: A survey," *Neurocomputing*, vol. 525, pp. 42–53, Mar. 2023, doi: 10.1016/j.neucom.2023.01.049.
[26] Y. Kwak, W. Joon Yun, J. Pyoung Kim, H. Cho, M. Choi, S. Jung, and J. Kim, "Quantum distributed deep learning architectures: Models, discussions, and applications," 2022, *arXiv:2202.11200*.
[27] V. Kulkarni, S. Pawale, and A. Kharat, "A classical-quantum convolutional neural network for detecting pneumonia from chest radiographs," 2022, *arXiv:2202.10452*.
[28] S. Maurizio, "Encoding techniques for quantum machine learning," M.S. thesis, Dept. Electron. Eng., Politecnico di Torino, 2022.
[29] S. Moradi, C. Brandner, C. Spielvogel, D. Krajnc, S. Hillmich, R. Wille, W. Drexler, and L. Papp, "Clinical data classification with noisy intermediate scale quantum computers," *Sci. Rep.*, vol. 12, no. 1, p. 1851, Feb. 2022, doi: 10.1038/s41598-022-05971-9.
[30] E. H. Houssein, Z. Abohashima, M. Elhoseny, and W. M. Mohamed, "Hybrid quantum-classical convolutional neural network model for COVID-19 prediction using chest X-ray images," *J. Comput. Des. Eng.*, vol. 9, no. 2, pp. 343–363, Feb. 2022, doi: 10.1093/jcde/qwac003.
[31] J. Amin, M. A. Anjum, M. Sharif, S. Jabeen, S. Kadry, and P. Moreno Ger, "A new model for brain tumor detection using ensemble transfer learning and quantum variational classifier," *Comput. Intell. Neurosci.*, vol. 2022, pp. 1–13, Apr. 2022, doi: 10.1155/2022/3236305.
[32] V. Azevedo, C. Silva, and I. Dutra, "Quantum transfer learning for breast cancer detection," *Quantum Mach. Intell.*, vol. 4, no. 1, p. 5, Jun. 2022, doi: 10.1007/s42484-022-00062-4.
[33] J. Amin, M. Sharif, N. Gul, S. Kadry, and C. Chakraborty, "Quantum machine learning architecture for COVID-19 classification based on synthetic data generation using conditional adversarial neural network," *Cognit. Comput.*, vol. 14, no. 5, pp. 1677–1688, Sep. 2022, doi: 10.1007/s12559-021-09926-6.
[34] E. Ovalle-Magallanes, J. G. Avina-Cervantes, I. Cruz-Aceves, and J. Ruiz-Pinales, "Hybrid classical–quantum convolutional neural network for stenosis detection in X-ray coronary angiography," *Exp. Syst. Appl.*, vol. 189, Mar. 2022, Art. no. 116112, doi: 10.1016/j.eswa.2021.116112.
[35] G. Spadarella, T. Perillo, L. Ugga, and R. Cuocolo, "Radiomics in cardiovascular disease imaging: From pixels to the heart of the problem," *Current Cardiovascular Imag. Rep.*, vol. 15, no. 2, pp. 11–21, Feb. 2022, doi: 10.1007/s12410-022-09563-z.
[36] I. Cetin, Z. Raisi-Estabragh, S. E. Petersen, S. Napel, S. K. Piechnik, S. Neubauer, M. A. Gonzalez Ballester, O. Camara, and K. Lekadir, "Radiomics signatures of cardiovascular risk factors in cardiac MRI: Results from the UK biobank," *Frontiers Cardiovascular Med.*, vol. 7, Nov. 2020, Art. no. 591368, doi: 10.3389/fcvm.2020.591368.
[37] D. A. Shoieb et al., "CAT-Seg: Cascaded medical assistive tool integrating residual attention mechanisms and Squeeze-Net for 3D MRI biventricular segmentation," *Phys. Eng. Sci. Med.*, vol. 15, 2023, doi: 10.1007/s13246-023-01352-2.
[38] A. Bahl, B. Hellack, M. Balas, A. Dinischiotu, M. Wiemann, J. Brinkmann, A. Luch, B. Y. Renard, and A. Haase, "Recursive feature elimination in random forest classification supports nanomaterial grouping," *NanoImpact*, vol. 15, Mar. 2019, Art. no. 100179, doi: 10.1016/j.impact.2019.100179.
[39] *Qiskit Textbook*. Accessed: Nov. 3, 2023. [Online]. Available: https://qiskit.org/learn
[40] D. Thukaram, H. P. Khincha, and H. P. Vijaynarasimha, "Artificial neural network and support vector machine approach for locating faults in radial distribution systems," *IEEE Trans. Power Del.*, vol. 20, no. 2, pp. 710–721, Apr. 2005, doi: 10.1109/TPWRD.2005.844307.
[41] *Quantum Neural Networks—Qiskit Machine Learning 0.6.1 Documentation*. Accessed: Nov. 3, 2023. [Online]. Available: https://qiskit.org/ecosystem/machine-learning/tutorials/01_neural_networks.html
[42] *Quantum-Enhanced Support Vector Machine (QSVM)—Qiskit 0.24.1 Documentation*. Accessed: Nov. 3, 2023. [Online]. Available: https://qiskit.org/documentation/stable/0.24/tutorials/machine_learning/01_qsvm_classification.html
[43] K. He, X. Zhang, S. Ren, and J. Sun. (2015). *Deep Residual Learning for Image Recognition*. [Online]. Available: http://image-net.org/challenges/LSVRC/2015/

DOAA A. SHOIEB received the B.Sc. and M.Sc. degrees in computer engineering from Arab Academy for Science, Technology and Maritime Transport (AASTMT), in 2014 and 2016, respectively. She is currently an Assistant Lecturer with the Department of Computer Engineering, AASTMT. Her current research interests include medical image analysis, machine learning, and quantum computing.

AHMED YOUNES received the Ph.D. degree from the University of Birmingham, U.K., in 2004. He is currently a Professor of computer science with Alexandria University and an Honorary Research Fellow with the School of Computer Science, University of Birmingham. He is also the Founder and the Leader of the Alexandria Quantum Computing Group. He has published many articles in *Quantum Algorithms* journal and *Reversible Circuits* journal.

SHERIN M. YOUSSEF received the M.Sc. and Ph.D. degrees in intelligent distributed systems from the University of Nottingham, England, U.K., in 2004. She is currently a Professor and the Head of the Computer Engineering Program, Arab Academy for Science and Technology and Maritime Transport (AASTMT). She is also a member of the scientific committee of many international journals, a Technical Committee of the WSEAS International Conference on Computer Engineering and Applications and the International IASTED Conference and a Technical Reviewer of the IEEE International Conference on Intelligent Systems and the International Conference on Computer Theory and Applications. She is leading many research groups in video surveillance systems, biomedical engineering, video and image compression, electronic watermarking, information hiding, network security, vision analysis, and automated spy navigating robots.

KARMA M. FATHALLA (Member, IEEE) received the M.Sc. degree from the Arab Academy for Science and Technology and Maritime Transport (AASTMT), Egypt, and the Ph.D. degree in machine learning from Aston University, U.K. During her studies as a Researcher, she presented her work in several reputable conferences and high impact factor journals. She is currently an Associate Professor with the Department of Computer Engineering, AASTMT. Her research interests include data mining, signal and image processing, pattern recognition, multimodal signal processing, health informatics, and machine learning.